arXiv:1107.1960v1 [cond-mat.supr-con] 11 Jul 2011

Fermi-Surface Reconstruction Involving Two Van Hove Singularities across the Antiferromagnetic Transition in $BaFe_2As_2$

Y. Nakashima,[1,2] A. Ino,[1,2] S. Nagato,[1,2] H. Anzai,[3] H. Iwasawa,[3] Y. Utsumi,[1,2]
H. Sato,[2,3] M. Arita,[3] H. Namatame,[3] M. Taniguchi,[1,3] T. Oguchi,[4]
Y. Aiura,[2,5] I. Hase,[5] K. Kihou,[2,5] C. H. Lee,[2,5] A. Iyo,[2,5] and H. Eisaki[2,5]

[1] *Graduate School of Science, Hiroshima University, Higashi-Hiroshima 739-8526, Japan*
[2] *JST, Transformative Research-Project on Iron Pnictides (TRIP), Chiyoda, Tokyo 102-0075, Japan*
[3] *Hiroshima Synchrotron Radiation Center, Hiroshima University, Higashi-Hiroshima 739-0046, Japan*
[4] *Institute of Scientific and Industrial Research, Osaka University, Ibaraki, Osaka 567-0047, Japan*
[5] *National Institute of Advanced Industrial Science and Technology, Tsukuba 305-8568, Japan*

(Dated: July 12, 2011)

We report an angle-resolved photoemission study of $BaFe_2As_2$, a parent compound of iron-based superconductors. Low-energy tunable excitation photons have allowed the first observation of a saddle-point singularity at the Z point, as well as the Γ point. With antiferromagnetic ordering, both of these two van Hove singularities come down below the Fermi energy, leading to a topological change in the innermost Fermi surface around the k_z axis from cylindrical to tear-shaped, as expected from first-principles calculation. These singularities may provide an additional instability for the Fermi surface of the superconductors derived from $BaFe_2As_2$.

PACS numbers: 74.70.Xa, 74.25.Jb, 71.18.+y

For newly-discovered iron-based superconductors [1], essential ingredients are considered to be inherited from antiferromagnetic (AF) parent compounds. Starting from a 122-type $BaFe_2As_2$, carrier doping, pnictogen substitution, or pressure application gives rise to a superconducting (SC) phase out of an AF metallic phase. Both these phase transitions evolve from Fermi-surface instabilities. For example, the nesting of the Fermi surfaces induces some density-wave orders along with the gap opening, and thus the nesting condition for the collinear AF order has been examined [2–5]. Another typical instability occurs near a van Hove singularity (vHS)—a sharp edge in the density of states (DOS), arising from a stationary point of band dispersion [6, 7]. There, a slight energy shift of the vHS is enough to reduce the DOS at the Fermi level (E_F) for stabilization, and concomitantly to change the topology of the Fermi surface. One aspect of the AF ordering instabilities is described in terms of spin fluctuation as a candidate for SC pairing interactions. Therefore, the Fermi surfaces of the parent compounds are the most fundamental to exploring the driving forces for the AF and SC phase transitions.

However, despite intensive studies on the AF phase of the 122-type systems, the three-dimensional (3D) shapes of the Fermi surfaces are controversial. Reports to date may be categorized into two groups. In the first, perpendicular-momentum (k_z) dependence is quite similar to that given by first-principles calculations for the non-magnetic (NM) state [8, 9], except for the Brillouin-zone (BZ) folding due to the AF order and some minor corrections. Specifically, for the innermost Fermi surface around the k_z axis, the cross-section area monotonically increases in going from the $k_z = 0$ to the $k_z = 2\pi/c$ plane bounding the BZ, as reported by many angle-resolved photoemission (ARPES) studies using conventional excitation-photon energies within $h\nu = 25 - 105$ eV [3–5, 10–13]. In the second, by contrast, totally reconstructed 3D Fermi surfaces are predicted by first-principles calculations for the collinear AF state [9, 14–16]. This picture is qualitatively consistent with quantum-oscillations data [14–16], and was also suggested in a laser-based low-energy ARPES report on a certain k_z plane using $h\nu = 7$ eV [17]. Between the contrasting ARPES reports, a considerable difference exists in the excitation-photon energy $h\nu$, because the typical probing depth increases from ∼5 to ∼20 Å, when $h\nu$ is decreased from ∼50 to ∼13 eV [18], in addition to the improvement in momentum resolution [19]. Therefore, a k_z-dependent low-energy ARPES study is needed for conclusive clues to the bulk Fermi surfaces.

In this Letter, we report the 3D shapes of the Fermi surfaces of $BaFe_2As_2$, using ARPES spectra taken by sweeping $h\nu$ in a low-energy range from 6.5 to 30 eV. In stark contrast to the previous ARPES results, the innermost Fermi surface around the k_z axis shows a non-monotonic k_z dispersion. Our observations on two saddle points show that two vHSs are involved in the Fermi-surface reconstruction across the AF transition and possibly affect the Fermi-surface instabilities.

High-quality single crystals of $BaFe_2As_2$ were grown by a flux method, as described in Ref. 20. ARPES measurements were performed at a helical undulator beamline, BL-9A of the Hiroshima Synchrotron Radiation Center (HRSC), using a Scienta R4000 electron analyzer. Total energy and momentum resolution was typically 12 meV and 0.01 Å^{-1}, respectively, for $h\nu = 13$ eV. The samples were cleaved *in situ* and kept under ultra-high vacuum better than 4×10^{-11} Torr during the measure-

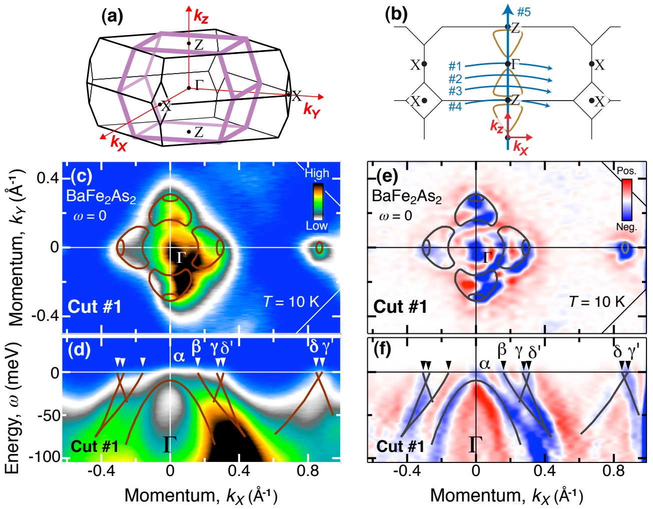

FIG. 1: (a) Notation of point labels and axes. Thick purple and thin black lines denote the Brillouin zones (BZs) with and without AF order, respectively. (b) Cutting paths #1-#5 in a schematic $k_Y = 0$ plane. (c),(d) Fermi-surface mapping and energy-momentum distribution of ARPES intensity in the AF state at $T = 10$ K, taken along cut #1 through Γ. (e),(f) Same as in (c) and (d), but filtered by k_X-k_Y Laplacian. Curves denote the Fermi surfaces and band dispersions determined from Laplacian analysis.

ments. First-principles density-functional calculations were performed using an all-electron full-potential linear augmented-plane-wave method. Although the BZ of BaFe$_2$As$_2$ should be folded back under the collinear AF order below $T_N = 134$ K, we use the labels of the unfolded tetragonal BZ throughout this paper as shown in Fig. 1(a), and define the Γ-X direction as along the k_X axis. The in-plane cuts #1-#4, which intersect the k_z axis at $k_z c/4\pi = 3.00$, 2.86, 2.69 and 2.50 as shown in Fig. 1(b), were taken with $h\nu = 23$, 20, 16.5 and 13 eV, respectively, where we adopted a free-electron final-state approximation and determined an inner potential of 13.6 eV from the perpendicular cut #5 presented in Fig. 2(c5).

In the AF state at $T = 10$ K, the folding of BZ was indeed observed in the in-plane cuts. In Figs. 1(d) and (f), three hole-pocket-like bands and an electron-pocket-like band are observed around Γ, and labeled α, β, γ and δ', respectively. The dispersions near X are labeled γ' and δ, which are almost identical to those of γ and δ', respectively, when shifted in momentum by a vector connecting Γ and X. This indicates the BZ folding due to the AF order, and we ascribed δ' and γ' to the replica bands, since they are unexpected from the NM calculations [8, 9]. Figures 1(c) and (e) show complicated flower-like Fermi surfaces, revealing that the band structure is further reconstructed by hybridization, as recognized previously [11, 17, 21]. Here, the fourfold symmetry is due to the coexistence of structural twin domains [22].

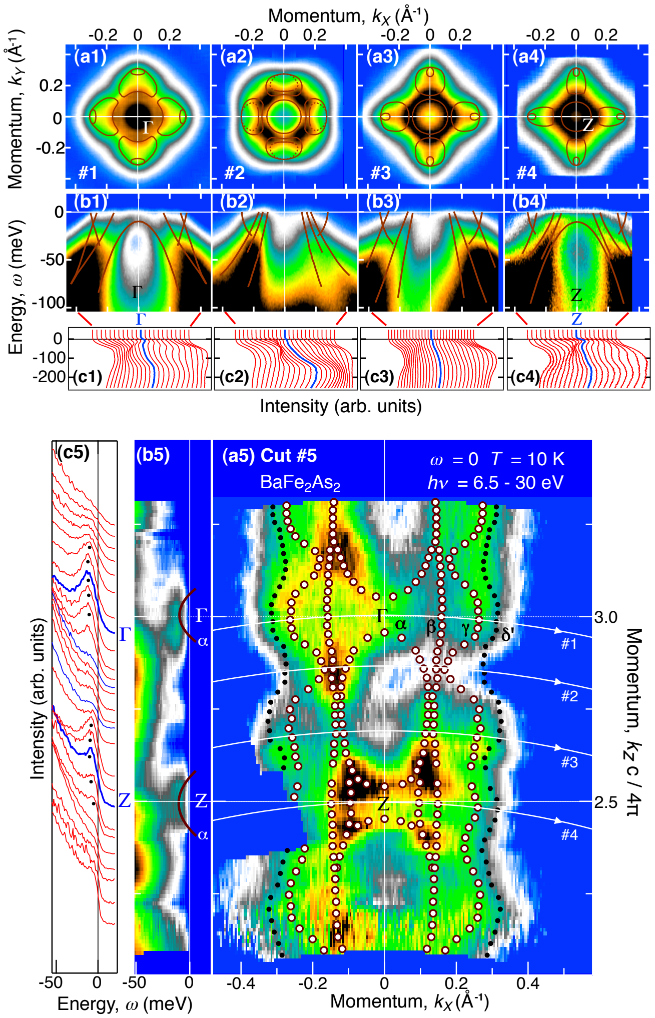

FIG. 2: (a1)-(a4) Fermi-surface mappings along the in-plane cuts #1-#4 indicated in Fig. 1(b). The intensity maps have been symmetrized with respect to the $k_X = 0$ and $k_X = k_Y$ lines. (a5) Fermi-surface mapping along the perpendicular cut #5 ($k_Y = 0$ plane). (b1)-(b5) Energy-momentum distribution images along the cuts #1-#5. (c1)-(c5) Energy distribution curves along the cuts #1-#5.

Comparing the in-plane cuts #1-#4, one finds dramatic k_z dependence in the AF state. In particular, the innermost hole pocket α shows non-monotonic k_z dispersion in contrast to the conventional ARPES results [3–5, 10–13]. In Figs. 2(c1)-(c4), a dispersive peak remains below E_F at Γ for cut #1 and at Z for cut #4, while it crosses E_F and disappears for cuts #2 and #3, as highlighted with blue curves. In Figs. 2(b1)-(b4), the top of the α pocket is distinctly observed below E_F for cuts #1 and #4, while it is gone above E_F for cuts #2 and #3. In Figs. 2(a1)-(a4), the intensity distribution is seen to peak at the center of the BZ for cuts #1 and #4, while it forms a ring-shaped peak for cuts #2 and #3.

The perpendicular cut #5 complements our 3D perspective. We identified Γ and Z as the saddle points of the α band, because Figs. 2(b5) and (c5) show that

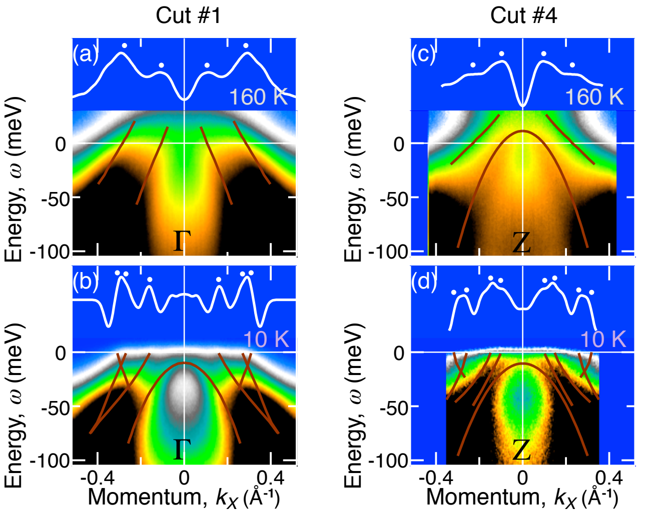

FIG. 3: Energy-momentum distributions of ARPES intensity above and below the AF transition $T_{\rm N} = 138$ K, symmetrized with respect to the $k_X = 0$ line. Second derivative of logarithmic momentum distribution curve at $\omega = 0$ is also shown as a white curve at the top of each panel. (a),(b) Cut #1 through Γ taken at $T = 160$ and 10 K. (c),(d) Cut #4 through Z taken at $T = 160$ and 10 K. The data at $T = 160$ K were divided by a Fermi-Dirac distribution function.

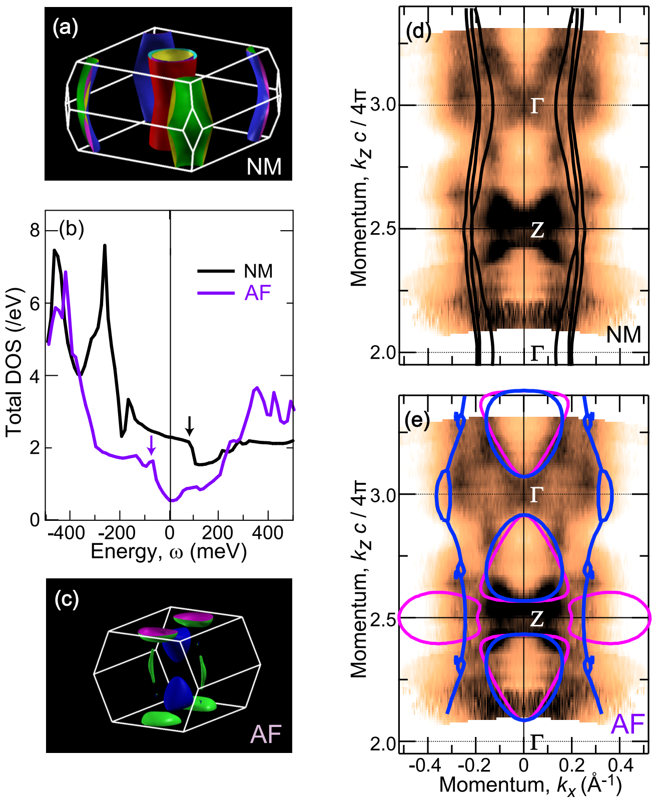

FIG. 4: Results of first-principles calculation for nonmagnetic (NM) and collinear antiferromagnetic (AF) states. (a),(c) Perspective views of the Fermi surfaces for the NM and AF states. (b) Total DOS for the NM (black) and AF (violet) states. The vHSs near $E_{\rm F}$ are indicated by arrows. (d),(e) Cross-sectional views of the Fermi surfaces for the NM and AF states, overlaid on the ARPES intensity map along cut #5. Blue and purple curves denote the distinct sheets along the twin axes for the AF state.

the bottoms of the k_z dispersion are at Γ and Z, where the top of the in-plane dispersion is located. The clear Fermi-surface crossings seen in Figs. 2(b5) and (c5) indicate that the innermost Fermi surface is separated into tear-shaped hole pockets as traced out in Fig. 2(a5). The present k_z mapping in Fig. 2(a5) exhibits more dispersive features than those reported previously [3–5, 10–13]. Not only the α pocket, but also the γ segment of a Fermi surface is tightly curved around the Γ point. Nevertheless, at the majority of k_z values, the γ and δ' segments are close to each other, suggesting that the nesting is still realized between them. This explains why only the γ' and δ' bands are visible among possible replicas.

These saddle-point energies are indeed involved in the AF phase transition, as can be seen from Fig. 3. When the temperature is raised across $T_{\rm N}$, both the Γ and Z saddle points have gone above $E_{\rm F}$ as shown in Figs. 3(a) and (c), respectively. These results imply that the transition to the AF phase is accompanied by a topological change in the innermost Fermi surface from cylindrical to tear-shaped. In addition, Fig. 3 also shows that the δ' band disappears above $T_{\rm N}$, verifying its dependence on the AF order.

The observed Fermi-surface reconstruction exhibits the same tendency as that expected from the first-principles calculation shown in Figs. 4(a) and (c). The tear-shaped α pocket in Fig. 2(c5) is well reproduced by the calculation for the collinear AF state in Fig. 4(c), and is consistent with the quantum-oscillations results [14–16]. In Fig. 2(c5), it appears that α splits near Z into sheets that are parallel and perpendicular to the k_z axis, in keeping with the two distinct sheets predicted along the twin axes. As shown in Fig. 4(d), the ARPES intensity distribution is far from the Fermi surfaces calculated for the NM state. In Fig. 4(e), by contrast, it resembles those for the AF state in the inner α pocket, and also the outer band γ at $k_X \sim 0.26$ Å^{-1} shows the intense portions reminiscent of the cigar-shaped pockets in the calculation. On the other hand, some discrepancies still remain. For example, petal-shaped Fermi surfaces were observed in all the in-plane cuts #1-#4 [Figs. 2(a1)-(a4)], while they are expected only for cut #4 from the calculation [Fig. 4(c)]. We cannot exclude the possibility that some unpredicted Fermi surfaces are the remnants of surface-state signals. More probably, the discrepancies are associated with the fact that the magnetic moment yielded by the calculation, $1.58\mu_{\rm B}$ per Fe site, is substantially larger than the experimental value, $0.93\mu_{\rm B}$, determined by neutron diffraction [23]. Accordingly, it is reasonable to assume that the magnitude of the AF gap was also overestimated in the calculation. Thus, the reality would

TABLE I: Energy, ω_{SP}, and effective masses, $m_\parallel$ and $m_\perp$, of Γ and Z saddle points, determined by the ARPES experiment and the first-principles calculation for $\mathrm{BaFe_2As_2}$. The effective masses are deduced from the dispersion curvatures along the in-plane and perpendicular directions, and given in unit of free-electron mass, m_{e}.

	Γ(exp.)	Γ(calc.)	Z(exp.)	Z(calc.)
ω_{SP} (meV)	−10(2)	−12	−10(2)	−82
$m_\perp/m_{\mathrm{e}}$	1.2(8)	1.3	1.7(9)	0.21
$-m_\parallel/m_{\mathrm{e}}$	3.5(6)	0.68[a]	4.0(6)	>20[a]
		1.9[b]		2.9[b]

[a] k_X direction in Fig. 1(a).

[b] k_Y direction in Fig. 1(a).

fall somewhere between the simply-folded Fermi surfaces and the fully-reconstructed ones shown in Fig. 4(c).

Next, we characterize the Γ and Z saddle points and their impacts on the DOS as vHSs. Qualitatively, the experiment and the calculation agree that they come down below E_{F} with the AF transition, suggesting that this behavior contributes to the stabilization of the AF order. Quantitatively, some energetic renormalizations are deduced from Table I. In comparison with the first-principles calculation, the experimental in-plane dispersion curvature for Γ is flattened by a factor of 2 or 5, and, more strikingly, both the k_z-dispersion curvature and the saddle-point energy for Z are renormalized by as much as a factor of $\sim$8. Their dominance in low-energy electronic states is characterized by the momentum-integrated DOS. As shown in Fig. 4(b), the calculated DOS sharply drops near E_{F} to about one third in the AF state. It follows from the above renormalizations that the actual singularities in the DOS become even higher, sharper and closer to E_{F}.

These findings provide a new perspective on the fluctuations towards the collinear AF order in 122-type superconductors. Previously, the nesting instabilities of the outer Fermi surfaces has been explored extensively [2–5, 12, 13]. Also for the present results, the $\gamma - \delta$ nesting seems plausible along a majority of k_z values. On the other hand, the absence of nesting has been reported for another iron-based superconductor LiFeAs [24]. Besides the nesting, we suggest an instability of the innermost Fermi surface. In view of the dominance of the vHSs, the Γ and Z saddle points would have a considerable tendency to sink below E_F. In other words, the cylindrical α sheet has an intrinsic tendency towards the tear-shaped Fermi surface. In light of the concept of electron-nematic phase transition, the Fermi-surface instability towards the spontaneous rotational-symmetry breaking, called Pomeranchuk instability, would be enhanced specifically by involving a vHS, as has been argued for the superconducting mechanism in cuprates [6, 7, 25, 26].

Finally, we briefly address what allowed us to observe more detailed k_z dispersions than the previous works [3–5, 10–13]. Most likely, the probing depth was increased by using low-energy excitation photons, because, in principle, this makes the experimental k_z better defined and increases the fraction of the bulk signal. In fact, some characteristic features, such as the saddle-point behavior at Z, are shared among the results of the present work and other bulk-sensitive studies [14–17]. So we speculate that the magnetic and electronic states may be affected at the sample surface, and that the k_z dispersion of the iron-based superconductors should be revisited.

In conclusion, our low-energy ARPES study of $\mathrm{BaFe_2As_2}$ has revealed that the 3D Fermi-surface reconstruction across the AF transition is more drastic than expected from conventional ARPES. The innermost hole pocket topologically changes from cylindrical to tear-shaped, involving two vHSs dominant near E_{F}. The possible role of the vHS-induced instability in the 122-type superconductors needs to be addressed in depth by future experimental and theoretical studies.

We acknowledge discussions with K. Shimada, and technical support from J. Jiang and H. Hayashi. This work was supported by KAKENHI (20740199). The ARPES experiments were done under the approval of HSRC (Proposal No. 09-A-1 and 10-A-14).

[1] Y. Kamihara *et al.*, J. Am. Chem. Soc. **130**, 3296 (2008).
[2] V. B. Zabolotnyy *et al.*, Nature (London) **457**, 569 (2009).
[3] C. Liu *et al.*, Phys. Rev. Lett. **102**, 167004 (2009).
[4] W. Malaeb *et al.*, J. Phys. Soc. Jpn. **78**, 123706 (2009).
[5] S. Thirupathaiah *et al.*, Phys. Rev. B **81**, 104512 (2010).
[6] C. J. Halboth and W. Metzner, Phys. Rev. Lett. **85**, 5162 (2000).
[7] H. Zhai *et al.*, Phys. Rev. B **80**, 064517 (2009).
[8] G. Xu *et al.*, Europhys. Lett. **84**, 67015 (2008).
[9] F. Ma *et al.*, Front. Phys. China **5**, 150 (2010).
[10] P. Vilmercati *et al.*, Phys. Rev. B **79**, 220503 (2009).
[11] M. Yi *et al.*, Phys. Rev. B **80**, 174510 (2009).
[12] T. Kondo *et al.*, Phys. Rev. B **81**, 060507 (2010).
[13] Q. Wang *et al.*, arXiv:1009.0271.
[14] S. E. Sebastian *et al.*, J. Phys. Condens. Matter **20**, 422203 (2008).
[15] J. G. Analytis *et al.*, Phys. Rev. B **80**, 064507 (2009).
[16] T. Terashima *et al.*, arXiv:1103.3329.
[17] T. Shimojima *et al.*, Phys. Rev. Lett. **104**, 057002 (2010).
[18] M. P. Seah and W. A. Dench, Surf. Interface Anal. **1**, 2 (1979).
[19] T. Yamasaki *et al.*, Phys. Rev. B **75**, 140513 (2007).
[20] M. Nakajima *et al.*, Phys. Rev. B **81**, 104528 (2010).
[21] G. Liu *et al.*, Phys. Rev. B **80**, 134519 (2009).
[22] M. A. Tanatar *et al.*, Phys. Rev. B **79**, 134528 (2009).
[23] Q. Huang *et al.*, Phys. Rev. Lett. **101**, 257003 (2008).
[24] S. V. Borisenko *et al.*, Phys. Rev. Lett. **105**, 067002 (2010).
[25] E. Fradkin and S. A. Kivelson, Science **327**, 155 (2010).
[26] T. M. Chuang *et al.*, Science **327**, 181 (2010).